AMERICAN METEOROLOGICAL SOCIETY

Journal of Climate

EARLY ONLINE RELEASE

The DOI for this manuscript is doi: 10.1175/JCLI-D-12-00580.1

The final published version of this manuscript will replace the preliminary version at the above DOI once it is available.

If you would like to cite this EOR in a separate work, please use the following full citation:

NOBRE, P., L. Siqueira, R. de Almeida, M. Malagutti, E. Giarolla, G. Castelão, M. Bottino, P. Kubota, S. Figueroa, M. Costa, M. da Silva, L. Irber, and G. Marcondes, 2013: Climate Simulation and Change in the Brazilian Climate Model. J. Climate. doi:10.1175/JCLI-D-12-00580.1, in press.

Climate Simulation and Change in the Brazilian Climate Model

Paulo Nobre[1], Leo S. P. Siqueira, Roberto A. F. de Almeida, Marta Malagutti, Emanuel Giarolla, Guilherme P. Castelão, Marcus J. Bottino, Paulo Kubota, Silvio N. Figueroa, Mabel C. Costa, Manoel Baptista Jr., Luiz Irber Jr., Gabriel G. Marcondes

National Institute for Space Research – INPE,
Cachoeira Paulista, SP, Brazil

Submitted to J. Climate on 31 July 2012
Revised form on 21 December 2012

[1] *Corresponding author address*: Paulo Nobre, National Institute for Space Research – INPE, Rodovia Presidente Dutra, Km 40, Cachoeira Paulista, SP 12630-000, Brazil. e-mail: paulo.nobre@cptec.inpe.br

Abstract

The response of the global climate system to atmospheric CO_2 concentration increase in time is scrutinized employing the Brazilian Climate Model (BESM-OA2.3). Through the achievement of over two thousand years of coupled model integrations in ensemble mode, it is shown that the model simulates the signal of recent changes of global climate trends, depicting a steady atmospheric and oceanic temperature increase and corresponding marine ice retreat. The model simulations encompass the time period from 1960 to 2105, following the Coupled Model Intercomparison Project 5 (CMIP5) protocol. Notwithstanding the accurate reproduction of large scale ocean-atmosphere coupled phenomena, like the ENSO phenomena over the Equatorial Pacific and the interhemispheric gradient mode over the Tropical Atlantic, the BESM-OA2.3 coupled model shows systematic errors on sea surface temperature and precipitation which resemble those of other global coupled climate models. Yet, the simulations demonstrate the model's potential to contribute to the international efforts on global climate change research, sparking interest in global climate change research within the Brazilian climate modeling community, constituting a building block of the Brazilian Framework for Global Climate Change Research.

1. Introduction

The conclusions of the Intergovernmental Panel on Climate Change (IPCC) Assessment Report No. 4 (IPCC 2007) are unequivocal regarding the human interference on the global climate via the buildup of Green House Gases (GHG) into the atmosphere. The steady increase of GHG concentration in the atmosphere, CO_2 being the most notable of them, has led the scientific community and Governments alike to debate the issue to exhaustion. Therefore, a detailed scrutiny of the influence of atmospheric GHG concentration on the climate system is a must and has been delved in by several research groups worldwide. Such scrutiny is presently applied to matters ranging from the development of state-of-the-art coupled climate models up to complex earth system models (ESM) which incorporate the complexity of the many components of the earth system. Examples of such complex system models are those developed by the largest climate research centers in the world, such as the National Center for Atmospheric Research – NCAR's CCSM4 (Bates et al. 2012; Grodsky et al. 2012), Geophysical Fluid Dynamics Laboratory – GFDL's CM2.3 (Delworth et al. 2012), and the Hadley Centre's HadGEM-ES. Yet, other climate centers around the world are also developing their own climate models, either by adapting a particular state-of-the-art global ESM, or by combining ocean, atmosphere, and surface component models from various sources; creating their "own" global climate model. This is the path chosen by Brazil, which has decided to develop its ESM, whose initial steps are underway and are detailed in this article.

The effort to develop Brazil's ESM is part of a national coordinated effort to build a multidisciplinary research framework geared at understanding the causes of global

56 climate change, its effects, and impacts on society. In this coordinated effort, the
57 Brazilian National Institute for Space Research (INPE) is leading the construction of a
58 global climate model capable of predicting the consequences of the buildup of GHG in
59 the atmosphere. This article describes the first version of this model, here represented by
60 the global ocean-atmosphere coupled model, named Brazilian Earth System Model –
61 Ocean-Atmosphere version 2.3 (BESM-OA2.3). For this article, we have followed the
62 criteria for participation in the Coupled Models Intercomparison Project 5 (CMIP5)
63 protocol (Taylor et al. 2009), aiming at simulating the behavior of the coupled ocean-
64 atmosphere system on decadal time scales under varying GHG concentrations in the
65 atmosphere.

66 In so doing, we have developed a model which is capable of performing seasonal
67 to decadal predictions, moving in the direction of a seamless prediction system (Palmer et
68 al. 2008; Shukla 2009), as other centers have already embraced worldwide. With this goal
69 in mind, this article presents the ability of BESM-OA2.3 to simulate global trends and
70 global climate variability related to historical variations of GHG concentrations in the
71 atmosphere. Such exercise constitutes a benchmark of the model's capability to be used
72 for studies involving more complex phenomena in the future.

73 BESM-OA2.3 is an evolution of previous versions of the Brazilian Center for
74 Weather Forecasting and Climate Studies (CPTEC) coupled ocean-atmosphere model,
75 which have been used to study the impacts of Amazon deforestation on climate (Nobre et
76 al. 2009), the dynamics of the South Atlantic Convergence Zone (SACZ) over cold
77 waters (Chaves and Nobre 2004; Nobre et al. 2012), the importance of ocean-atmosphere
78 coupling to represent the Atlantic thermocline depth (Siqueira and Nobre 2006), as well

as for regional seasonal predictions with the Eta regional model over South America (Pilotto et al. 2012). All these studies highlighted the importance of ocean–atmosphere coupling to better predict the phenomena of study.

The challenge in this article is to demonstrate that the coupled ocean-atmosphere model developed at INPE is suitable to simulate climate phenomena along the last few decades and into the near future, for the period from 1960 to 2035. This article shows that the model is capable of reproducing global trends of ocean heat content and top- of-atmosphere radiation balance, as well as important modes of climate variability. The effects of observed variations of atmospheric CO_2 during the period of study and its projection into the near future are also investigated. Regardless of the simplicity of BESM-OA2.3 compared to full ESMs (*e.g.*, Muñoz et al. 2012; Delworth et al. 2012), its results are comparable to other global climate models.

2. Model description

The BESM-OA2.3 coupled climate model used in this research is constituted by the CPTEC/INPE Atmospheric General Circulation Model (AGCM) coupled to GFDL's MOM4p1 Oceanic General Circulation Model (OGCM) via GFDL's Flexible Modular System. The component models and coupling are described as follows.

Atmosphere model

The CPTEC/INPE AGCM has been constantly modified during the last few years. The implementation of two new dynamic cores (Eulerian and Semi-Lagrangian) and the

algorithm for the use of a reduced grid are now employed operationally at CPTEC. For the present work, the Eulerian core and reduced grid have been used. The options for physical parameterizations include the Simplified Simple Biosphere (SSiB) module surface (Xue et al. 1991), turbulence level 2 module (Mellor and Yamada 1982), gravity wave module (Anthes 1977), deep convection module (Arakawa and Shubert 1974; Grell and Devenyi 2002), shallow convection module (Tiedtke 1984), short-wave radiation CLIRAD-SW-M (Tarasova et al. 2006, Chou and Suarez 1999), longwave module (Hashvardhan and Corsetti 1984; Hashvardhan et al 1987), and the model for interaction of radiation with clouds (Slingo, 1987; Hou, 1990; Kinter et al. 1997). In the shortwave and longwave radiation schemes the carbon dioxide is globally specified, assuming either a 370 ppm fixed value (for the control integrations, labeled "physics2" for the CMIP5 protocol) or a time dependent function (transient integrations, "physics1").

The new deep convection scheme implemented in the CPTEC–AGCM is based on the convective parameterization developed by Grell and Devenyi (2002), hereafter referred as Grell-ensemble (GRE) scheme. This scheme includes several alternative closure assumptions to estimate the cloud base mass flux. Both the first type of closure (Grell closure) and the second type (Arakawa-Schubert closure) assume a quasi-equilibrium state between large-scale forcing and convection. Other closures used are the Kain-Fritsch closure, in which the atmospheric stability is removed by the convection within the specified convective time, moisture convergence closure, and low level vertical velocity mass flux closure. The set of convection scheme ensembles used in the CPTEC-AGCM includes 144 different versions of the cumulus parameterization, 16 from dynamic control and 9 from static control. The details of implementation of this scheme

in the CPTEC-AGCM and its impact on tropical precipitation can be found in Figueroa et al. (2012).

The exchanges of heat, moisture, and momentum between the surface and atmosphere in the CPTEC–AGCM over the ocean and continents are computed differently by various physical processes that define the surface fluxes. The model uses an empirical relationship that approximates the theory of Monin–Obukhov similarity to determine the transfer and the drag coefficient. The relationships over the ocean differ from those over land. Over the oceans, the momentum, heat, and moisture fluxes are parameterized considering the global aerodynamic scheme (bulk aerodynamic schemes) where the fluxes are assumed to be proportional to wind speed and the surface potential (difference in temperature or moisture between the ocean surface and the air near the surface). The proportionality or drag coefficient is calculated by an empirically determined functional fit. On the surface of the ocean the functional fit is similar to the one used by Sato et al. (1989). With regard to momentum, heat, and moisture fluxes over the continent, the parameterization used is more sophisticated. The surface scheme on the continent considers a variety of different types of vegetation, soil, and geographical formation. The Simplified Simple Biosphere (SSiB) (Xue et al. 1991) scheme used in the CPTEC–AGCM, despite being a simplified model, has many physical processes that represent the interactions between land surface and atmosphere.

The AGCM has spectral horizontal resolution truncated at triangular wave number 62, which gives an equivalent grid size of 1.875 degrees, and 28 sigma levels unevenly spaced in the vertical (i.e. T062L28).

Ocean model

The ocean model used in this work is the "Modular Ocean Model - MOM4p1 (Griffies 2009) from GFDL, which includes the Sea Ice Simulator – SIS built-in ice model (Winton 2000). The horizontal grid resolution is set to 1^o in the longitudinal direction, and in the latitudinal direction the grid spacing is $1/4^o$ in the tropical region (10^oS–10^oN) decreasing uniformly to 1^o at 45^o and to 2^o at 90^o of both hemispheres. For the vertical axis, 50 levels are adopted with a 10-m resolution in the upper 220 m, increasing gradually to about 370 m of grid spacing at deeper regions. The variant of the ocean model not coupled to an atmospheric model, here referred to as "OGCM" or "forced" model, is forced by winds, temperature, specific humidity at 10 m, sea level pressure, radiative fluxes, sea ice cover and thickness, and river discharges. The OGCM spinup was done in a manner similar to that used by Nobre et al. (2012): starting from zero currents velocities and Levitus (1982) T-S structure of the world ocean, running the forced model for 13 years with climatological atmospheric forcing fields, followed by an additional 58 years (1950–2007) forced by interannual fields from Large and Yeager (2009); except for river discharges and the sea ice variables, which were kept climatological in both cases. During the forced model run, the dynamic and thermodynamic structure of the ocean was saved at regular periods of time in order to be used as initial states of the ocean for the coupled model experiments.

The model settings are similar to the COREs experiment settings (Griffies and coauthors 2009) apart from modifications made to obtain better results for our forced and coupled experiments at the chosen ocean grid, such as changing the smoothing of the sea surface height ("laplacian" instead of "biharmonic"), disabling the "mixing downslope"

module (which treats the mixing of tracer between dense shallow parcels and deeper parcels downslope), disabling the tidal forcing module, enabling the "convect" module (which vertically adjusts gravitationally unstable columns of ocean fluid), changing parameters of the frazil module (which computes the heating of seawater due to frazil ice formation), disabling the restoring masks, as well as other restoring options, with the exception of the salinity restoring which is kept on with a time scale of 60 days. The turbulent flux calculation described by Large and Yeager (2009) is used in the forced model in order to compute the surface drag coefficients.

The coupled version of the ocean model has additional changes in relation to the forced model. The background vertical diffusivity was defined by the Bryan Lewis scheme (Bryan and Lewis, 1979), zonally constant, but varying both meridionally and vertically. Between 10^{o}N and 10^{o}S, the Bryan Lewis diffusion coefficient span from $2x10^{-5}$ m^2/s near the surface to $7.8x10^{-5}$ m^2/s at the bottom. Such values increase linearly poleward to compensate for the coarser grid, measuring $2.3x10^{-5}$ m^2/s at the surface and $8.7x10^{-5}$ m^2/s at the bottom near the poles. The consequent near surface eddy kinetic energy is coherent with the observations (not shown), considering the limitations of the simulations setup. The BESM-OA2.3 simulations develop up to 1.2 cm^2/s^2 average eddy kinetic energy over a few degrees around the equator. This value rapidly decays poleward due to the gradually coarser grid resolution near the poles. Moreover, in the coupled model all restoring options including the salinity restoring are disabled.

Coupling strategy

The coupled model uses GFDL's Flexible Modeling System (FMS) coupler to couple the CPTEC–AGCM to GFDL MOM 4p1 (Griffies 2009) and SIS (Winton 2000). The main characteristics of the CPTEC–AGCM are described in the previous subsection. The original configuration of MOM4p1 is similar to that used in the COREs release of the model for the forced experiments using Large and Yeager (2009) fields. For the coupled model, all restore flags were turned off. Wind stress fields are computed, using Monin–Obukhov scheme within MOM4p1, from the wind field 10 meters above the ocean surface. Adjustments were done to the Monin–Obukhov boundary layer scheme, whose parameters were tuned according to the wind fields output by the CPTEC-AGCM. The hydrological cycle is balanced by an indirect method, as suggested in Griffies (2010). The AGCM receives the following two fields from the coupler: sea surface temperature (SST) and ocean albedo from ocean and sea ice models at an hourly rate (coupling time step). Adjustments were also made to ocean shortwave penetration parameters due to the CTPEC-AGCM supply of visible and infrared short wave radiation. The coupling variables supplied by the AGCM are: fresh water (liquid and solid precipitation), specific humidity, heat, vertical diffusion of velocity components, momentum fluxes, and surface pressure.

Experiment design

The numerical experiments design followed the CMIP5 protocols (Taylor et al. 2009) for decadal, short term simulations, and near future predictions using two types of physics for the coupled model differing on the concentration of atmospheric CO_2. Integrations

labeled "physics1" used atmospheric CO_2 concentrations derived from *in situ* air samples collected at Mauna Loa Observatory, Hawaii. Historical data from Bacastow et al. (1985) were regressed onto a parabolic equation defined by:

$$CO_2 = a\,t^2 + b\,t + c$$

where the CO_2 concentration is in ppm, t is the number of fractional years since 2000, a=0.0116696, b=1.79984, and c=369. Integrations labeled "physics2" used atmospheric CO_2 concentrations fixed at 370 ppm and are referred to as control run throughout the text.

Ensemble members were integrated for 10 years each with Initial Conditions (IC) on 1–10 December of years: 1960, 1965, 1970, 1975, 1980, 1985, 1990, 1995, 2000, and 2005, for each physics1 and physics2. Three of these ensembles, namely, 1960, 1980, and 2005, were extended for an extra 20 years for each of the ten members, completing 30 years long integrations each, referred in the text as decadal runs, and an extra 70 years for only the IC conditions of 1st December, completing 100 years long single simulations, referred in the text as centennial runs, respectively. In addition, one member CMIP5 "1pct-co2" run was computed, assuming a 1% yearly increase in the atmospheric CO_2 concentration, starting at the 20th year of the 1960, physics2 run and completing 80 years.

The CPTEC-AGCM initial conditions for each ensemble member used the National Centers for Environmental Prediction/National Center for Atmospheric Research (NCEP/NCAR) reanalysis fields (Kalnay et al. 1996) for the 00:00 GMT of each day from 1st to 10th of December of the chosen years. The ocean initial states were

chosen for the same dates from a spinup run of MOM4p1 that used prescribed atmospheric fields of momentum, solar radiation, air temperature, and fresh water described earlier in this section.

The outputs from the ocean model were generated directly at the proper frequencies requested according to the CMIP5 experiment specification. The atmospheric data were output at a three hourly frequency and later processed using the CMOR2 software (Doutriaux and Tayler 2011) to satisfy all CMIP5 output requirements.

3. Results

Atmospheric CO2 concentration, Ocean Heat content and TOA fluxes

The residual SST between the physics1 experiment and the physics2 control run show a uniform global SST warming for the 100-years long experiments (Figure 1a) showing a trend of 0.054 K/decade ($p<0.01$). This corresponds to approximately 50% of the observed global SST warming in the 1980-2011 period, as estimated from averaging Hadley Centre HadSST2 anomalies globally (figure not shown).

The propagation of the CO_2–induced extra heat into the surface layers of the ocean can be illustrated in Figure 1b, which shows the global average physics1 minus physics2 mean temperature as a function of depth and time for the centennial2005 run. It is noteworthy in Figure 1b the surface warming penetrating characteristic with warmer physics1 ocean during the 2005–2105 period. The residual temperature propagation due to atmospheric CO_2 concentration changes reach the upper 400m of the oceans in approximately 50 years. Such ocean warming is consistent with the global ice reduction shown in Figure 1c in terms of physics1–physics2, acting to reduce the surface albedo.

Yet, the analysis of decadal trends in SST are only weakly indicative of changes in the top- of- atmosphere radiation balance (TOA). The importance of ocean heat content (OHC) as a diagnostic for changes in the climate system has been emphasized in many recent papers (Domingues et al. 2008; Levitus 2012; Palmer et al. 2011). Trends in total ocean heat content strongly constrain TOA since the ocean is the primary heat store in the Earth System. The essential balance in the Earth System is between total OHC (the primary heat storage term) and F_{TOA} (the total radiation flux entering or leaving the system). Therefore, we use conservation of energy to write the following equation

$$F_{TOA}\ t\ = \frac{1}{A_{earth}} \frac{dH_o}{dt}\ (W\ m^{-2}), \quad (1)$$

where $F_{TOA}\ t$ is the net inward radiative flux through the top of the atmosphere, A_{earth} is the area of the Earth, and H_o is the ocean heat content.

Numerous assumptions underlie this equation, particularly the neglect of the thermal energy of the other components of the climate system (atmosphere, land, cryosphere, and geothermal fluxes). Therefore, changes in OHC should approximately balance the time integrated TOA. Climate modeling and observations indicate that to understand the global energy budget fully, one needs to include measurements of the deep oceans in the OHC analysis. The surface layers, even down to 700 meters, are not robust indicators of total OHC, although the OHC-700m is strongly correlated (though not perfectly) to the TOA imbalance.

The key questions here is whether this CO_2–induced extra heat into the oceans is indicative of changes in the Earth's top- of- atmosphere radiation balance, and thus an

282 increase of the accumulation of energy in the Earth System. Figure 2a shows the full
283 depth ocean heat content anomaly (OHCA) of the centennial2005 (physics1 minus
284 physics2) runs. This global average show a steady rise, to the end of the 100yr, of the full
285 depth ocean heat content for the centennial2005 (physics1) relative to the control run
286 with fixed CO_2 (physics2).

287 In order to assess the energy flux change on the top of the atmosphere due to
288 different CO_2 forcing conditions, we compute the top-of-atmosphere radiation flux
289 imbalance (TOA) implied by the ocean heat content difference in terms of its trend over
290 the 100 years period shown in Figure 2b. The estimated trend in TOA for the 2005-2105
291 period is of $+0.3 W/m^{-2}$ per year represented by the red dashed line in Figure 2b. In a
292 recent determination of OHC for the 0-2000 m layer, Levitus et al. 2012 report an
293 implied rate in TOA of $+0.27\ W/m^{-2}$ per unit area of earth's surface for the 1955-2010
294 period.

295 The radiative flux change on the top of the atmosphere due to different CO_2
296 forcing conditions can be affected by changes in clouds radiative forcing (e.g., Senior
297 1999; Stephens 2005). Radiative feedbacks involving low level clouds are a primary
298 cause of uncertainty in global climate model projections (IPCC 2007). In order to
299 investigate the low cloud responses to climate perturbations, we computed the time series
300 of global low cloud cover physics1–physics2 runs during the 2005-2105 period. The
301 increase in atmospheric CO_2 concentration in BESM-OA2.3 model produces a small
302 change in low cloud cover, around 0.1 % increase over 100 years (figure not shown). The
303 result is in accordance with other cloud responses to climate perturbations studies (Wyant
304 et al. 2006; Williams et al. 2006).

The results in this subsection indicate that there are mechanisms operating in the BESM-OA2.3 climate model that are capable of re- distributing substantial quantities of heat at all depths of the ocean on decadal time scale due to changes in atmospheric CO_2 concentration.

The Atlantic Meridional Overturning Circulation

The BESM-OA2.3 is able to reproduce the Atlantic Meridional Overturning Circulation (AMOC), a fundamental process in the Atlantic Ocean. North Atlantic Deep Water (NADW) is formed on the north Atlantic and exported southward below 1000m, while a warmer near surface flow closes the system determining a northward net heat transport (Talley 2003). Figure 3 shows the meridional spatial pattern of the AMOC as represented by the BESM-OA2.3 and obtained from the average along 25 years (from year 95 to 120 of physics2 centennial run) of the vertical cumulative sum of the zonal total transport for each depth and longitude. In other words, each point shows the average meridional total transport through a section along that longitude, from that depth up to the surface. The upper 1000m in the Atlantic basin is dominated by a northward transport up to 35°N. Between 1000 and 3500m the cumulative transport reduces as a consequence of the southward NADW, while below 3500 the Antarctic Bottom Water flows northward.

The BESM-OA2.3 not only reproduces the 3 layer meridional overturning circulation system, but also well determines its intensity. Probably the best estimate of the AMOC has been done by the RAPID-MOC, an observing array system along the 26.5°N cross section operating since 2004, suggesting a transport of 18.5 ± 4.9 Sv (Johns et al. 2011). At the same section, the BESM-OA2.3 reproduces a maximum transport of

approximately 20 Sv, slightly higher than, but still within the uncertainty of the observations.

The most impressive point is that this is the preferred stable state of the model. The small frame in Figure 4 shows the maximum AMOC transport throughout the 122 years elapsed after the spinup, *i.e.*, once the coupled model runs free with physics2 configuration (constant atmospheric CO_2 concentration). The transport is initially just below 10 Sv, nearly half of the observed value, but it continually increases until stabilizing at approximately 20 Sv, after 80 years. There were no prescribed forcing driving to this result, except for the model internal dynamics. The adequate adjustment of the AMOC reproduced on the BESM-OA2.3, despite the bias from the spinup, is a strong argument that the model is capturing the main Earth system processes, and hence should be a good approximation of reality.

Model climatology and systematic errors

SST AND PRECIPITATION ANNUAL BIASES

In order to evaluate the ability of BESM-OA2.3 to reproduce the observed climate, the annual biases of SST and precipitation were computed and contrasted with the biases for other three CMIP5 global models, namely; Hadley Centre Coupled Model version 3 (HadCM3), NCAR's CCSM4 coupled model, and the Canadian CanCM4 coupled model. The Optimal Interpolation SST (OISST) dataset, combining *in situ* and satellite SST interpolated onto a one-degree grid with weekly resolution (Reynolds et al. 2002), was used to assess the SST biases; while the CPC Merged Analysis of Precipitation (CMAP), constructed from gauge observations, satellite estimates, and numerical model outputs

(Xie and Arkin 1998) was used to evaluate the precipitation biases. Both datasets were averaged in time, resulting in global maps of climatological values.

The annual mean SST biases relative to OISST are presented in Figure 5. The results indicate that the BESM-OA2.3 model has an extensive negative SST bias over the tropical and subtropical oceans (Figure 5a), much like both the HadCM3 model (Figure 5b) and the CanCM4 model (Figure 5d). The exception is on the eastern boundaries of the Pacific and Atlantic Ocean, where the models are unable to properly reproduce the tilt of the equatorial thermocline (not shown), resulting in a warm bias of approximately 2 K. The pattern of a colder tropical North Atlantic and a hotter tropical South Atlantic is related to wind stress biases and has also been observed in other models (Muñoz et al., 2012). Bottino and Nobre (2012) have studied the impact of cloud cover parameterizations on BESM-OA2.3, obtaining a reduction of the North Atlantic cold bias and South Atlantic warm bias on this model.

The most outstanding cold bias occurs in the simulation of the North Atlantic in all four CMIP5 models in Figure 5, which is also similar to GFDL CM2.5 (Delworth et al. 2012), since both CM2.5 and BESM-OA2.3 coupled models share the same ocean component; and on the Southern Ocean, where warm biases are predominant much like the NCAR CCSM4 model (Figure 5a,c). The model overestimates SSTs by as much as 3 K in eastern boundary currents (e.g. Humboldt, California, and Benguela currents). One possible explanation for the spatial extent and magnitude of the warm bias in the eastern currents is that it results from positive feedback between the processes involved in the formation of marine stratocumulus clouds over cold waters and their cloud shading effect

373 reducing the net surface radiative forcing (Ma et al. 1996, Siqueira and Nobre 2006,
374 Zheng et al. 2011).

375 The SST biases in BESM-OA2.3 show no significant variation when biases from
376 the ensemble mean of individual experiments decadal1960, decadal1980, and
377 decadal2005 are intercompared. The biases are also indifferent to CO_2 values, displaying
378 no significant difference between the physics1 and physics2 integrations (figures not
379 shown). These results suggest that the observed biases in SST are essentially determined
380 by the model formulation.

381 Annual mean precipitation biases are shown in Figure 6, following the same
382 approach used for SST. While the BESM-OA2.3 model is able to reproduce global
383 observed values of precipitation, it displays biases that arise from the inability to position
384 the ITCZ (Intertropical Convergence Zone) correctly, a common feature of all the four
385 CMIP5 models in Figure 6. The Tropical Pacific is characterized in BESM-OA2.3 by a
386 double ITCZ and a missing SPCZ (South Pacific Convergence Zone) (Figure 6a). The
387 Tropical Atlantic is better reproduced and although the ITCZ is shifted towards the south,
388 the SACZ (South Atlantic Convergence Zone) has an improved representation compared
389 to its Pacific counterpart. These deficiencies, of the double ITCZ in the Pacific and the
390 southward shift of the ITCZ in the Atlantic, are known problems of current global models
391 (Lin 2007; Richter and Xie 2008).

392 The biases originated from not representing the ITCZ properly include an excess
393 of precipitation over the South Atlantic Ocean, Indian Ocean, and most of the South
394 Pacific Ocean, with the exception of the SPCZ region. The Equatorial Pacific and
395 northern Tropical Atlantic are characterized by negative biases in precipitation, while

most of the North Pacific and North Atlantic Oceans show positive biases. Over land, the strongest signal comes from the Amazon basin, where the model is characterized by negative biases, similar to the HadCM3 (Figure 6b) and CanCM4 (Figure 6d) models. These biases are caused by the reduced convection over the Amazon forest and are possibly connected to the SST biases via the Walker circulation over the Atlantic Ocean, through trade winds, and the tilt of the equatorial thermocline (Braconnot et al. 2007; Breugem et al. 2008; Richter and Xie 2008; Tozuka et al. 2011). In earlier versions of the coupled ocean-atmosphere model (e.g. Nobre et al. 2009), base for the BESM-OA coupled model, the trade winds over the Atlantic Ocean had their direction reversed during part of the year, producing strong positive SST biases when the equatorial thermocline collapsed, reducing convection over land. This has been improved in the current version of the model, mostly due to the Grell-ensemble cummulus parameterizations used (Grell and Devenyi 2002), although some bias still remain. Similar to the SST, precipitation biases are time and physics invariant, showing no significant differences between periods or CO_2 physics.

Figure 7 shows the seasonal cycle in the deviations of SST at the equator about the annual mean for OISST and four current CMIP5 models (top panel). The variation in observed SST is dominated by the annual harmonic that peaks at about 100^{o}W, with the warm phase in April slightly stronger than the cold phase in September-October (Figure 7a). All four models fail to capture the correct start and duration of the warm phase (Fig7b-e). The main part of seasonal variation in equatorial SST is realistically located over the eastern Pacific in all four models, although deviations are concentrated too close to the coast for BESM-OA2.3 (Figure 7b) or extend too far west as in CanCM4 (Figure

7e). The seasonal cycle is quite weak in HadCM3 and CCSM4 (Fig7.c-d) and the simulated SSTs are correctly dominated by the annual harmonic, except in BESM-OA2.3 for which the semi-annual harmonic is the dominant feature (Figure 7b).

In order to investigate to what extent convection is taking place south of the equator in the eastern Pacific and its seasonality, Hovmöller diagrams of precipitation for CMAP and four current CMIP5 models averaged from 100^{o}W to 150^{o}W are also plotted in Figure 7 (bottom panel). The rainfall from CMAP observations is largely confined to an ITCZ located between 5^{o}N and 15^{o}N (Figure 7f). The seasonal variation in latitude for the observations is small with the ITCZ reaching 15^{o}N around September and its southern-most position in March-April, almost reaching the equator. The rainfall maximum simulated by the BESM-OA2.3 model has realistic magnitude, but the precipitation is severely overestimated south of the equator (much like CSSM4 and CanCM4 in Figure 7i-j) and produces a rather persistent double ITCZ throughout the year (Figure 7g).

Interannual variability

EL NIÑO–SOUTHERN OSCILLATION

The spatial patterns of tropical interannual SST variability for the BESM-OA2.3 model and observations are shown in Figure 8. The BESM-OA2.3 model exhibits weaker equatorial Pacific variability than that observed in recent decades, correctly placing the center of the Pacific SST variability relative to the observed pattern, although with too little variability along the coast of Peru. It is worth noting that the tropical Atlantic SST simulations also show weaker interannual SSTA fluctuations than the observations.

442 The ENSO variability is frequently characterized by indexes of SST variability
443 for specific regions over the equatorial Pacific, however the SST and wind patterns may
444 differ among models and observation. Therefore, performing comparisons can be
445 difficult. Nobre and Shukla (1996), for example, discussed the tropical Atlantic ocean–
446 atmosphere variability through empirical orthogonal function (EOF) analysis (Lorenz
447 1956), joining the fields of SST and wind stress anomalies normalized by the local
448 standard deviation prior to the EOF calculations, a technique referred as "joint EOF" (or
449 "jEOF") analysis. Hence it is more convenient to characterize ENSO variability in terms
450 of joint EOF of the SST and wind stress fields so that the model's ENSO can be studied.
451 In this case, ENSO variability is considered to be represented by the leading jEOFs of
452 anomalous monthly SST and wind stress over a region that nearly spans the equatorial
453 Pacific, and by the time series of the corresponding principal components. In this
454 analysis, the jEOFs are normalized to have unit spatial variance, and hence the variances
455 of each principal component (PC) reflect spatiotemporal variances of corresponding SST
456 and wind stress anomalies, with variances of all the PCs summing to the total variance.
457 The jEOF analysis is presented in Figure 9, where (a) shows the first jEOF of observed
458 SSTs (Reynolds et al. 2002) and wind stress fields estimated with observed winds from
459 NCEP/NCAR reanalysis (Kalnay et al. 1996), from January 1950 to December 2010 (60
460 years).

461 The main pattern of variability associated with ENSO on the outputs of BESM-
462 OA2.3 physics2 centennial run with fixed atmospheric CO_2 concentration can be
463 determined through the first jEOF of monthly SSTs and wind stress, and is plotted in
464 Figure 9b for a 100 years period. The first jEOF (jEOF1) reflects the mature phases of the

ENSO life cycle, i.e., the mature phases of El-Niños and La-Niñas. Despite broadly resembling the observed variability (Figure 9a), we detect a strong meridional confinement of the SST anomalies around the equator and the center of action of this mode is displaced eastward when compared to the observations. The meridional confinement can be caused by a narrow meridional span of zonal wind stress anomaly and has implications in the interannual variability (Kirtman 1997, Deser et al. 2006). The first jEOF explains only 19% of variance, versus over 38% in the observations.

The first jEOF pattern of the BESM-OA2.3 model in the equatorial Pacific does not change significantly over the 100yr period for a twin physics1 simulation (not shown), suggesting that the ENSO variability is only affected in its characteristic period by weak global temperature increase.

The power spectra of the first principal component (PC1) for observed SST (solid black) and for the twin 100yr simulations starting at 2005 physics1 (solid red) and physics2 (solid blue) are shown in Figure 9c. The seasonal cycle and linear trends were removed when computing the jEOFs and the respective PCs to better isolate the modes of variability. The observed ENSOs have a relatively broad spectrum spanning 3–5 years. The model captures this feature qualitatively with peak ENSO period in BESM-OA2.3 at approximately 5 years, which is on the higher end of the 3-5 year band (towards lower frequencies). Changes in ENSO frequency under CO_2 increase can be noticed in Figure 9c (solid red) and an overall tendency for ENSO period to decrease is evident in accordance with Merryfield (2006) multimodel ensemble analysis.

Overall the model has a robust ENSO signal with multi-decadal fluctuations in amplitude (not shown), and an irregular period between 3 and 5 years with peak ENSO

period at approximately 5 years. The main ENSO pattern of SST variability simulated by the model is shifted about 30° east of the observed patterns, and the transition pattern matches the observations well with some deficiencies mainly over the equator (not shown). Such problems may be linked to the model mean state biases namely the equatorial cold bias, the double ITCZ, and the overstratified surface waters near the South American coast.

EXTRATROPICAL TELECONNECTIONS

The extratropical teleconnections are recurrent atmospheric circulation patterns associated with variations in the strength and location of the polar jet stream, the subtropical jet stream, or mid-latitude storm tracks (Chang and Fu 2002).

The Pacific-North American teleconnection pattern (PNA) is one of the most prominent and influential modes of low-frequency variability in the Northern Hemisphere mid-latitudes beyond the tropics (Wallace and Gutzler 1981). The PNA pattern features large-scale above-average surface pressure anomalies that arc from the Hawaiian Islands and over the intermountain region of North America, and below-average surface pressure located south of the Aleutian Islands and over the southeastern United States (Figure 10a).

The PNA pattern is associated with noticeable fluctuations in the strength and location of the East Asian jet stream. The positive phase is associated with an intensified East Asian jet stream, and with an eastward shift in the jet exit region toward the western United States. The negative phase is associated with a westward shrink of the jet stream toward eastern Asia, and blocking activity over the high latitudes of the North Pacific.

Although the PNA and ENSO are distinct natural internal modes of climate variability, the PNA has been found to be strongly influenced by the ENSO phase (Straus and Shukla 2002). The positive phase of the PNA pattern tends to be associated to El-Niños, and during La-Niñas, the PNA tends to be in the negative phase.

The BESM-OA2.3 model matches well the PNA pattern and its amplitude (Figure 10b) with the center of action over the intermountain region of North America shifted about 20° east of the observed pattern. This mode of climate variability explains 12% of variance in the model versus over 17% in the observations.

In the Southern Hemisphere (SH), there is also one prominent low-frequency mode in the extratropics that resembles the PNA pattern, which is characterized by a well-defined wave train extending from the central Pacific to Argentina, and is referred to as the Pacific–South American (PSA) pattern (Ghil and Mo 1991; Mo and Higgins 1998; Lau et al. 1994).

The center of action of Pacific-South American (PSA) teleconnection pattern is located in the west of the Antarctic Peninsula in the observations and comprises a wave-train of alternate positive and negative geopotential height (or pressure) anomalies across the South Pacific emanating from the tropics (Figure 11a).

It has been suggested that this teleconnection pattern that acts over South America impacts the South Atlantic Convergence Zone, which results in a regional seesaw pattern of alternating dry and wet conditions (Nogués-Paegle and Mo, 1997). The PSA has also been found to be influenced by ENSO conditions (Mo and Nogués-Paegle 2001).

The model simulations show two main centers of action instead of one, a negative center located in the west of the Antarctic Peninsula similar to observations, and another

with similar amplitude over the Antarctic Peninsula. This mode of climate variability in the SH explains 18% of variance in the model, versus over 14% in the observations.

TROPICAL ATLANTIC VARIABILITY

The Tropical Atlantic Variability (TAV) is characterized by two main modes of variability, an ENSO-like equatorial mode (Zebiak 1993) and an interhemispheric gradient mode (e.g. Nobre and Shukla 1996). This last mode, also referred as the "Atlantic dipole mode" or the "Atlantic meridional mode," is related to the cross-equatorial gradient of the SST anomalies and resultant migrations of the intertropical convergence zone. Consequently, it has an impact on rainfall over the tropical Atlantic, including the continental areas of the northeast Brazil and African's Sahel region, at interannual and decadal climate scales (Doi et al. 2010 and references therein).

Several studies have employed the technique of EOF analysis to study covariant patterns of variability over the Atlantic Ocean (Venegas et al. 1997; Weare 1977). According to Nobre and Shukla (1996), from 1963 to 1987 the first jEOF mode spatial pattern of SST and wind stress anomalies showed a zonal, dipole-like structure in both SST and wind stress anomalies over the Tropical Atlantic, suggesting that warmer SSTs are connected to weaker trade winds, and colder SSTs to stronger trade winds (Dommenget and Latif 2000). A similar analysis is presented in Figure 12a, considering observed SSTs (Reynolds et al. 2002) and wind stress fields of the NCEP/NCAR reanalysis, from January 1960 to December 2010 (51 years), where all linear trends and seasonal cycles were removed prior to the analysis. The spatial pattern of the first jEOF, accounting for 12.5% of the total variance (Figure 12a), shows that the structure of the

557 Tropical Atlantic variability described by Nobre and Shukla (1996) was sustained until
558 2010, with the dipole-like feature in the SST pattern, and analogous connections SST–
559 trade winds. The power spectrum analysis of the amplitude time series of this mode
560 (Figure 12c) reveals a low frequency oscillation, which is represented as the main peak at
561 11.75 years, confirming the decadal timescale behavior of this pattern as noticed by
562 Nobre and Shukla (1996).

563 The occurrence of SST biases in the tropical Atlantic is a common issue of
564 coupled models and, as discussed by Richter and Xie (2008) and Doi et al (2010), almost
565 all CMIP3 models show the zonal SST gradient along the equator opposite to what is
566 observed. This deviation is possibly attributed to the lack of the cold tongue in the
567 equatorial Atlantic in many coupled model simulations. Even recent coupled models,
568 with higher horizontal resolution and updated parameterizations present SST biases in the
569 eastern equatorial Atlantic and the Angola–Benguela area (Doi et al. 2012). The BESM-
570 OA2.3 model also has the SST bias in the tropical Atlantic as discussed before (Figure 5).
571 Notwithstanding, it is able to simulate the Atlantic dipole mode quite well. Figure 12b
572 shows the jEOF analysis results of the physics2 centennial run simulation, starting from
573 December 2005 and with fixed CO_2 concentration. The spatial patterns of SST and wind
574 stress anomalies are very similar to the ones for observed data (Figure 12a), except for
575 the region near the Gulf of Guinea, where the negative SST patterns are stronger and the
576 wind stress patterns are preferably from SE instead of from S–SW, reflecting the SST
577 biases and the consequent discrepancies in the trade wind anomalies over this region. The
578 main period of this simulated Atlantic dipole mode is 15 years (Figure 12c). For the twin
579 centennial simulation with increasing CO_2 of physics1, jEOF analysis of the resultant

simulation also shows a dipole structure (figure not shown) similar to Figure 12b, but with the period of maximum spectral energy density at 6.43 years (Figure 12c). Apparently, the variations of the atmospheric radiative balance caused by an increasing atmospheric CO_2 concentration act to increase the Atlantic dipole frequency. Yet, the mechanisms by which it occurs still have to be further investigated.

4. Summary and Conclusions

This article has explored the global features and regional aspects of the BESM-OA2.3 coupled model for climate change research. The numerical experiment design was set accordingly to the CMIP5 protocol and was aimed at explicitly revealing the model sensitivity to atmospheric CO_2 concentration increase, as a representation of the buildup of Green House Gases in the atmosphere. Extended runs with over 2,000 years of ensemble members were generated to scrutinize the model behavior for decadal climate variability and change. It was demonstrated that the BESM-OA2.3 model responds to increasing atmospheric CO_2 concentrations in a consistent manner. The model simulations showed changes in Earth's top- of- atmosphere radiation balance, an increase of the accumulation of energy in the Earth System, and associated global sea surface temperature increase and marine ice reduction.

In terms of annual biases, the simulations show some of the same characteristics of other global coupled ocean-atmosphere models, namely the double ITCZ and an almost absent SPCZ over the Pacific Ocean, in addition to the southward displacement of the Atlantic ITCZ. Concurrent with most global coupled ocean-atmosphere models, a warm SST bias is present along the western coasts of South America and Africa.

602 Regarding precipitation, the model shows excess rainfall over the oceans and deficiencies
603 over the continents, particularly over the Amazon basin.

604 The model biases showed no significant sensitivity to atmospheric CO_2
605 concentrations, suggesting that such biases are a consequence of more basic model
606 physics deficiencies. The excess rainfall over the oceans was diagnosed after the fact, and
607 a new formulation for water vapor surface fluxes over the ocean has been developed at
608 CPTEC, and will be tested in a future experiment. Yet, the BESM-OA2.3 simulations
609 presented an improved representation of the SACZ relative to previous versions of its
610 base coupled ocean-atmosphere model, which we interpret as a direct consequence of the
611 improvements on deep cumulus parameterizations used for this research.

612 On the interannual spectrum of climate variability, the simulations have shown a
613 robust ENSO signal over the equatorial Pacific Ocean, with peak energy in the 3 to 5 year
614 range, and a dipole-like pattern of SST and surface winds with peak energy on the
615 decadal scale in the Atlantic Ocean, in agreement with observations. However, for the
616 centennial model runs under increasing atmospheric CO_2 concentrations the coupled
617 ocean-atmosphere modes of variability over both the Pacific (e.g. ENSO) and the tropical
618 Atlantic (e.g. the meridional mode) presented signals of enhanced periodicity, which may
619 be an indication that under growing atmospheric CO_2 concentrations, interannual climate
620 variability may grow. The model also represented atmospheric teleconnections in close
621 agreement with observations, which is an important benchmark for its use for climate
622 variability and change research.

The BESM-OA2.3 model has been used for operational seasonal predictions at CPTEC and constitutes a building block on the Brazilian framework for climate change research – Rede CLIMA.

Acknowledgements

The authors acknowledge Dr. Felipe M. Pimenta for his contributions to the development of a previous version of BESM-OA. This research was partially funded by FAPESP grant No. 2009/50528-6, MCTI/FINEP grant No. 01.08.0405.00, and CNPq grant No. 550990/2011-9. The model integrations were done at INPE's CRAY XE6 supercomputer at INPE/CPTEC, funded by the Brazilian Network on Global Climate Change Research – Rede CLIMA, and FAPESP Program on Global Climate Change Research.

References

Anthes, R. A., 1977: A Cumulus Parameterization Scheme Utilizing a One-Dimensional Cloud Model. *Monthly Weather Review*, **105,** 270-286.

Arakawa, A., and W. H. Shubert, 1974: Interaction of a cumulus ensemble with the large-scale environment, Part I. *J. Atmos. Sci.*, **31,** 674-704.

Bacastow, R. B., C. D. Keeling, and T. P. Whorf, 1985: Seasonal amplitude increase in atmospheric CO_2 concentration at Mauna Loa, Hawaii, 1959-1982. *J. Geophys Res*, **90**, 10529-10540.

644 Bates, S. C., B. Fox-Kemper, S. R. Jayne, W. G. Large, S. Stevenson, and S. G. Yeager,
645 2012: Mean biases, variability, and trends in air-sea fluxes and SST in the
646 CCSM4. *J. Climate***,** in press.
647 Bottino, M. J. and P. Nobre, 2012: Impacts of cloud cover schemes on the simulation of
648 the Atlantic ITCZ seasonal cycle in a coupled ocean–atmosphere model.
649 Submitted JGR.
650 Braconnot, P., F. Hourdin, S. Bony, J. L. Dufresne, J. Y. Grandpeix, and O. Marti, 2007:
651 Impact of different convective cloud schemes on the simulation of the tropical
652 seasonal cycle in a coupled ocean-atmosphere model. *Clim. Dyn.*, **29**, 501-520.
653 Breugem, W.P., P. Chang, C. J. Jang, J. Mignot, and W. Hazeleger, 2008: Barrier layers
654 and tropical Atlantic SST biases in coupled GCMs, *Tellus Ser*. A, **60**, 885–897.
655 Bryan, K. and L. J. Lewis, 1979: A water mass model of the world ocean. *Journal of*
656 *Geophysical Research,* **84**, 2503–2517.
657 Chang, E. K. M., and Y.F. Fu, 2002: Inter-decadal variations in Northern Hemisphere
658 winter storm track intensity. *J. Climate*, **15**, 642-658.
659 Chaves, R. R., and P. Nobre, 2004: Interactions between the South Atlantic Ocean and
660 the atmospheric circulation over South America. *Geophys. Res. Lett*., **31**,
661 doi:10.1029/2003GL018647.
662 Chou, M.D., and M.J. Suarez, 1999: A solar radiation parameterization (CLIRAD-SW)
663 for atmospheric studies. NASA/TM- 1999-104606, M. J. Suarez, Ed., *Series on*
664 *Global Modeling and Data Assimilation*, **15**, 40 pp.
665 Delworth, Thomas L., and Coauthors, 2012: Simulated climate and climate change in the
666 gfdl cm2.5 high-resolution coupled climate model. *J. Climate,* **25**, 2755–2781.

667 Deser, C., A. Capotondi, R. Saravanan, and A. Phillips, 2006: Tropical Pacific and
668 Atlantic climate variability in CCSM3. *J. Climate*, **19** (11), 2451–2481.

669 Doi, Takeshi, Tomoki Tozuka, Toshio Yamagata, 2010: The Atlantic Meridional Mode
670 and Its Coupled Variability with the Guinea Dome. *J. Climate*,**23**, 455–475.
671 doi: http://dx.doi.org/10.1175/2009JCLI3198.1

672 Doi, Takeshi, Gabriel A. Vecchi, Anthony J. Rosati, Thomas L. Delworth, 2012: Biases
673 in the Atlantic ITCZ in Seasonal–Interannual Variations for a Coarse- and a High-
674 Resolution Coupled Climate Model. *J. Climate*, **25**, 5494–5511.
675 doi: http://dx.doi.org/10.1175/JCLI-D-11-00360.1

676 Dommenget, D., and M. Latif, 2000: Interannual to Decadal Variability in the Tropical
677 Atlantic. *Journal of Climate*, **13,** 777-792.

678 Domingues, C.M., J.A. Church, N.J. White, P.J. Gleckler, S.E. Wijffels, P.M. Barker and
679 J.R. Dunn, 2008. Improved estimates of upper-ocean warming and multi-
680 decadalsea-level rise. *Nature*, **453**,1090-1093,

681 Doutriaux, and Tayler: Climate Model Output Rewriter (CMOR) [Available online at
682 http://www2-pcmdi.llnl.gov/cmor/documentation/cmor-2-0-users-guide-html.]

683 Figueroa, S. N., and coauthors, 2012: Simple Shallow Cumulus Model and its impact on
684 Diurnal Cycle of precipitation in the Tropics simulated by Climate AGCM. *To be*
685 *submitted*.

686 Ghil, M., and K. C. Mo, 1991: Intraseasonal oscillations in the global atmosphere. Part II:
687 Southern Hemisphere. *J. Atmos. Sci*., **48**, 780–790.

688 Grell, G. A., and D. Devenyi, 2002: A generalized approach to parameterizing convection
689 combining ensemble and data assimilation techniques. *Geophys. Res. Lett.*, **29**.

690 Griffies, S. M., 2009, *Elements of MOM4p1*. GFDL Ocean Group Technical Report No.
691 6, NOAA/Geophysical Fluid Dynamics Laboratory, Dec 2009, 444 pp.,
692 http://www.gfdl.noaa.gov/fms.

693 Griffies, S. M., and coauthors, 2009: Coordinated ocean-ice reference experiments
694 (COREs). *Ocean Modelling*, **26,** 1-46.

695 Grodsky, S. A., J. A. Carton, S. Nigam, and Y. Okumura, 2012: Tropical Atlantic Biases
696 in CCSM4. *J. Climate***,** in press.

697 Harshvardhan, R. Davies, D. A. Randall, and T. G. Corsetti, 1987: A fast radiation
698 parameterization for general circulation models. *J. Geophys. Res.*, **92**, 1009-1016.

699 Harshvardhan and T. G. Corsetti, 1984: Longwave radiation parameterization for the
700 UCLA/GLAS GCM. NASA Technical Memorandum 86072, 65 pp.

701 Hou, Y. T., 1990: Cloud-Radiation-Dynamics Interation. Ph.D. Thesis, University of
702 Maryland, 209 pp.

703 IPCC, 2007: Contribution of Working Group I to the Fourth Assessment Report of the
704 Intergovernmental Panel on Climate Change, 2007.

705 _____, 2007. Climate change 2007: The physical Science basis. Contribution of
706 working group I to the assessment report of the Intergovernamental Panel on
707 Climate Change [Solomon, S., D. Qin, M. Manning, Z. Chen, M. Marquis, K.B.
708 Averyt, M. Tignor and H.L. Miller (eds.)]. Cambridge University Press,
709 Cambridge, United Kingdom and New York, NY, USA, 996 pp.

710 Johns, W. E., and Coauthors, 2011: Continuous, Array-Based Estimates of Atlantic
711 Ocean Heat Transport at 26.5¬∞N. *Journal of Climate*, **24,** 2429-2449.

712 Kalnay, E., and Coauthors, 1996: The NCEP/NCAR 40-Year Reanalysis Project. *Bull.*
713 *Amer. Meteor. Soc.*, **77**, 437–471. doi: http://dx.doi.org/10.1175/1520-
714 0477(1996)077<0437:TNYRP>2.0.CO;2

715 Kinter III J. L., David DeWitt, P. A. Dirmeyer, M. J. Fennessy, B. P. Kirtman, L. Marx,
716 E. K. Schneider, J. Shukla and D. Straus, 1997: The COLA Atmosphere-
717 Biosphere General Circulation Model Volume 1: Formulation, COLA Technical
718 Reports, 51, 46 pp.

719 Kirtman, B. P., 1997: Oceanic Rossby wave dynamics and the ENSO period in a coupled
720 model. *J. Climate*, **10**, 1690–1705.

721 Lau, M. K., P. J. Sheu, and I. S. Kang, 1994: Multiscale low-frequency circulation modes
722 in the global atmosphere. *J. Atmos. Sci*., **51**, 2753–2750.

723 Large, W. and S. Yeager, 2004: Diurnal to decadal global forcing for ocean and sea-ice
724 models: the data sets and flux climatologies. CGD Division of the National Center
725 for Atmospheric Research, *NCAR Technical Note*: NCAR/TN-460+STR.

726 _____, 2009: The global climatology of an interannually varying air–sea flux data
727 set. *Climate Dynamics*, **33**, 341-364.

728 Levitus, S., 1982: Climatological Atlas of the World Ocean. Professional Paper 13,
729 (NTIS PB83-184093), 173 pp.

730 Levitus, S., et al. (2012), World ocean heat content and thermosteric sea level change (0-
731 2000), 1955-2010, *Geophys. Res. Lett.*,doi:10.1029/2012GL051106.

732 Lin, Jia-Lin, 2007: The Double-ITCZ Problem in IPCC AR4 Coupled GCMs: Ocean–
733 Atmosphere Feedback Analysis. *J. Climate*, **20**, 4497–4525. doi:
734 http://dx.doi.org/10.1175/JCLI4272.1

735 Lorenz, E. N., 1956: Empirical Orthogonal Functions and statistical weather prediction,
736 Scientific Report No. 1, 49 pp.

737 Ma, C.-C., C. R. Mechoso, A. W. Robertson, and A. Arakawa, 1996: Peruvian stratus
738 clouds and the tropical Pacific circulation: A coupled ocean-atmosphere GCM
739 study. *J. Clim.*, **9**, 1635-1645.

740 Mellor, G. L., and T. Yamada, 1982: Development of a turbulence closure model for
741 geophysical fluid problems. *Reviews of Geophyis. and Space Physics*, **20,** 851-
742 875.

743 Merryfield, W.J., 2006: Changes to ENSO under CO_2 doubling in a multi-model
744 ensemble. *J. Climate*, **19**, 4009-. 4027, DOI: 10.1175/JCLI3834.1

745 Mo, K.C. and Higgins, R.W. (1998). The Pacific-South American modes and tropical
746 convection during the Southern Hemisphere winter. *Mon Wea Rev*, **126**, 1581–
747 1596.

748 _____, and J. Nogués-Paegle, 2001: The Pacific-South American modes and their
749 downstream effects. *Int. J. Climatol*., **21**, 1211-1229.

750 Muñoz, Ernesto, Wilbert Weijer, Semyon A. Grodsky, Susan C. Bates, Ilana Wainer,
751 2012: Mean and Variability of the Tropical Atlantic Ocean in the CCSM4*. *J.*
752 *Climate*, **25**, 4860–4882. doi: http://dx.doi.org/10.1175/JCLI-D-11-00294.1

753 Nobre, P., and J. Shukla, 1996: Variations of sea surface temperature, wind stress, and
754 rainfall over the tropical Atlantic and South America. *J. Climate*, **9**, 2464-2479.

755 Nobre, P., S. E. Zebiak, and B. P. Kirtman, 2003: Local and remote sources of Tropical
756 Atlantic Variability as inferred from the results of a hybrid ocean-atmosphere
757 coupled model. *Geophys. Res. Lett*, **30**, 8008-8015.

758 Nobre, P., R. A. F. De Almeida, M. Malagutti, and E. Giarolla, 2012: Coupled ocean-
759 atmosphere variations over the South Atlantic ocean. *J. Climate*, in press. DOI:
760 10.1175/JCLI-D-11-00444.1

761 Nobre, P., M. Malagutti, D. F. Urbano, R. A. F. d. Almeida, and E. Giarolla, 2009:
762 Amazon deforestation and climate change in a coupled model simulation. *J.*
763 *Climate*, **22**, 5686–5697.

764 Nogués-Paegle, and K. C. Mo, 1997: Alternating vwet and dry conditions over South
765 America during summer. *Mon. Wea. Rev.*, **125**, 279-291.

766 Palmer, M. D., D. J. McNeall, and N. J. Dunstone, 2011: Importance of the deep ocean
767 for estimating decadal changes in Earth's radiation balance. *GRL*, **38,** 13707-
768 13712.

769 Palmer, T. N., F. J. Doblas-Reyes, A. Weisheimer, and M. J. Rodwell, 2008: Toward
770 Seamless Prediction: Calibration of Climate Change Projections Using Seasonal
771 Forecasts. *Bull. Amer. Meteor. Soc*., **89**, 459-470.

772 Pilotto, I., S. C. Chou, and P. Nobre, 2012: Seasonal climate hindcasts with Eta model
773 nested in CPTEC coupled ocean-atmosphere general circulation model.
774 Theoretical and Applied Climatology.

775 Reynolds, R.W., N.A. Rayner, T.M. Smith, D.C. Stokes, and W. Wang, 2002: An
776 improved in situ and satellite SST analysis for climate. *J. Climate*, **15**, 1609-1625.

777 Richter, I., and S.-P. Xie, 2008: On the origin of equatorial Atlantic biases in coupled
778 general circulation models. *Climate Dynamics*, **31** (5), 587-598.

779 Sato, N.; Sellers, P.J.; Randall, D.A.; Schneider, E.K.; Shukla, J.; Kinter, J.L., Hou, Y.T.;
780 Albertrazzi, E. 1989: Implementing the simple biosphere model in a general
781 circulation model. *J. Atmos. Sci.*, **46**, p.2757-2782, 1989.

782 Senior, C. A., 1999: Comparison of mechanisms of cloud-climate feedbacks in GCMs. J.
783 *Climate,* **12**, 1480–1489.

784 Shukla, J., 2009: Seamless Prediction of Weather and Climate: A New Paradigm for
785 Modeling and Prediction Research. U. N. O. a. A. Administration, Ed.

786 Siqueira, L., and P. Nobre, 2006: Tropical Atlantic sea surface temperature and heat flux
787 simulations in a coupled GCM. *Geophys. Res. Lett*., L15708,
788 doi:10.1029/2006GL026528.

789 Slingo, J.M., 1987: The development of verification of a cloud prediction scheme for the
790 ECMWF model. *Quart. J. Roy. Meteor. Soc.*, **113,** 899-927.

791 Straus, D. M., and J. Shukla, 2002: Does ENSO force the PNA. *J. Climate*, **15**, 2340 -
792 2358.

793 Stephens, G. L., 2005: Cloud feedbacks in the climate system: a critical review. *J.*
794 *Climate*, **18**, 237–273.

795 Talley, L. D., 2003: Shallow, Intermediate, and Deep Overturning Components of the
796 Global Heat Budget. *Journal of Physical Oceanography*, **33,** 530-560.

797 Taylor, K. E., R. J. Stouffer, and G. A. Meehl, 2009: A Summary of the CMIP5
798 Experiment Design. [Available online at http://www-pcmdi.llnl.gov/.]

799 Tarasova, T.A., H.M.J. Barbosa, and S.N. Figueroa, 2006: Incorporation of new solar
800 radiation scheme into CPTEC GCM. *Tech. Rep. INPE-14052-NTE/371*, Instituto
801 Nacional de Pesquisas Espaciais, 53 pp. [Available online at
802 http://urlib.net/sid.inpe.br/iris@1915/2006/01.16.10.40.]

803 Tiedtke, M., 1984: The sensitivity of the time mean large-scale flow to cumulus
804 convection in the ECMWF model. *Workshop on convection in large-scale*
805 *numerical models.*, Shinfield Park, Reading, United Kingdon, ECMWF, 297-316.

806 Tozuka, T., T. Doi, T. Miyasaka, N. Keenlyside, and T. Yamagata, 2011: Key factors in
807 simulating the equatorial Atlantic zonal SST gradient in a coupled GCM. *J.*
808 *Geophys. Res.*, **116**, C06010, doi:10.1029/2010JC006717.

809 Venegas, S. A., L. A. Mysak, and D. N. Straub, 1997: Atmosphere -ocean coupled
810 variability in the south Atlantic. *J. Climate*, **10**, 2904-2920.

811 Wallace, J. M., and D. S. Gutzler, 1981: Teleconnections in the geopotential height field
812 during the Northern Hemisphere winter. *Mon. Wea. Rev.*, **109**, 784–812.

813 Weare, B. C., 1977: Empirical orthogonal analysis of Atlantic Ocean surface
814 temperatures. *Quart. J. R. Met. Soc.*, **103**, 467-478.

815 Williams, K.D., M.A. Ringer, C.A. Senior, M.J. Webb, B.J. McAvaney, N. Andronova,
816 S. Bony, J.-L. Dufresne, S. Emori, R. Gudgel, T. Knutson, B. Li, K. Lo, I. Musat,
817 J. Wegner, A. Slingo, and J.F.B. Mitchell, 2006: Evaluation of a component of the

cloud response to climate change in an intercomparison of climate models. *Clim. Dynam.*, **26**, 145-165, doi:10.1007/s00382-005-0067-7.

Winton, M., 2000: A reformulated three-layer sea ice model. *J. Atmos. Ocean. Tech*., **17**, 525-531.

Wyant, M. C., and Coauthors, 2006: A comparison of low-latitude cloud properties and their response to climate change in three AGCMs sorted into regimes using mid-tropospheric vertical velocity. *Climate Dyn*amics, **27**, 261–279.

Xie, P., and P. A. Arkin, 1998: Global monthly precipitation estimates from satellite-observed outgoing longwave radiation. *J. Climate*, **11,** 137-164.

Xue, Y., P. J. Sellers, J. L. K. III, and J. Shukla, 1991: A simplified biosphere model for global climate studies. *J. Climate*, **4,** 345-364.

Zebiak, S. E., 1993: Air-Sea interaction in the equatorial Atlantic region. *J. Climate*, **6**, 1567-1586.

Zheng, Yangxing, Toshiaki Shinoda, Jia-Lin Lin, George N. Kiladis, 2011: Sea Surface Temperature Biases under the Stratus Cloud Deck in the Southeast Pacific Ocean in 19 IPCC AR4 Coupled General Circulation Models. *J. Climate*, **24**, 4139–4164.

Figures Captions

Figure 1. Globally averaged, phsics1 minus physics2 residual time series for the centennial2005 runs for (a) Sea Surface Temperature (SST), the red line is the linear fit for the SST time series with acclivity of $+5.4 \times 10^{-2}$ K/decade, (b) Vertical profile of global ocean temperature (K), depicting the propagation of the temperature signal through depth, and (c) Sea ice extent (km^2), the red line is the linear fit for the ice extent time series, with declivity of -2.7×10^5 km^2/decade.

Figure 2. 100-year trend for the centennial2005 physics1 minus physics2 residuals in: (a) full depth Ocean Heat Content Anomaly (OHCA) and (b) top-of-atmosphere radiation flux imbalance FTOA implied by the ocean heat content.

Figure 3. Spatial pattern of the Atlantic Meridional Overturning Circulation averaged along 25 years, from year 95 to 120 of centennial1960 physics2 run. This is the vertically cumulative sum of the total zonal transport.

Figure 4. Temporal variability of the maximum of the Atlantic meridional overturning Circulation on the BESM-OA2.3 along 25 years of simulation for the centennial1960 physics2 run. The smaller frame shows the same maximum along 125 year after the spinup, larger frame shows the temporal variability of the maximum.

858 Figure 5. Sea surface temperature bias in (a) BESM-OA2.3, (b) Hadley Centre Coupled
859 Model version 3 (HadCM3), (c) NCAR's CCSM4 coupled model, and (d) Canadian
860 CanCM4 coupled model. Units are in K.
861
862 Figure 6. Precipitation bias in (a) BESM-OA2.3, (b) Hadley Centre Coupled Model
863 version 3 (HadCM3), (c) NCAR's CCSM4 coupled model, and (d) Canadian CanCM4
864 coupled model. Units are in mm/day.
865
866 Figure 7. The seasonal cycle in equatorial SST (2^{o}S-2^{o}N) in terms of deviations from the
867 respective annual mean in ^{o}C for: (a) OISST, (b) BESM-OA2.3, (c) HadCM3, (d)
868 CCSM4, and (e) CanCM4. The seasonal cycle in precipitation over the eastern Pacific
869 (averaged between 150^{o} and 100^{o}W) plotted against latitude in mm/day for: (f) CMAP,
870 (g) BESM-OA2.3, (h) HadCM3, (i) CCSM4, and (j) CanCM4.
871
872 Figure 8. Standard deviation of SST anomalies (°C) over the tropics. (a) Observations
873 from ERSSTv3b, years 1950-2010, and (b) BESM-OA2.3 centennial2005 physics2
874 control run.
875
876 Figure 9. First jEOF of SST–Taux–Tauy monthly anomalies in the equatorial Pacific for
877 (a) observations, for the period 1960-2010, and (b) BESM-OA2.3 centennial2005,
878 physics2 control run for the period of the last 90 years of a 100-years run. (c) Power
879 spectra of the monthly PCs time series from observations in solid black, BESM-OA2.3
880 centennial2005 physics2 in solid blue, and BESM-OA2.3 centennial2005 physics1, in

881 solid red. Theoretical red noise spectrum is in dashed blue, 95% confidence level in
882 dotted blue.
883
884 Figure 10. The PNA teleconnection pattern of positive and negative monthly mean
885 surface pressure anomalies. Second sea level pressure EOF for (top) NCEP-NCAR
886 CDAS1 and (bottom) BESM-OA2.3 centennial2005 physics2 run.
887
888 Figure 11. The PSA teleconnection pattern of positive and negative monthly mean 500-
889 hPa height anomalies. Second 500mb geopotential thickness EOF for (top) NCEP-NCAR
890 CDAS1 and (bottom) BESM-OA2.3 centennial2005 physics2 run.
891
892 Figure 12. Same as Figure 9, but for the Tropical Atlantic between 30 S – 30 N, 70W –
893 20 E.
894

895

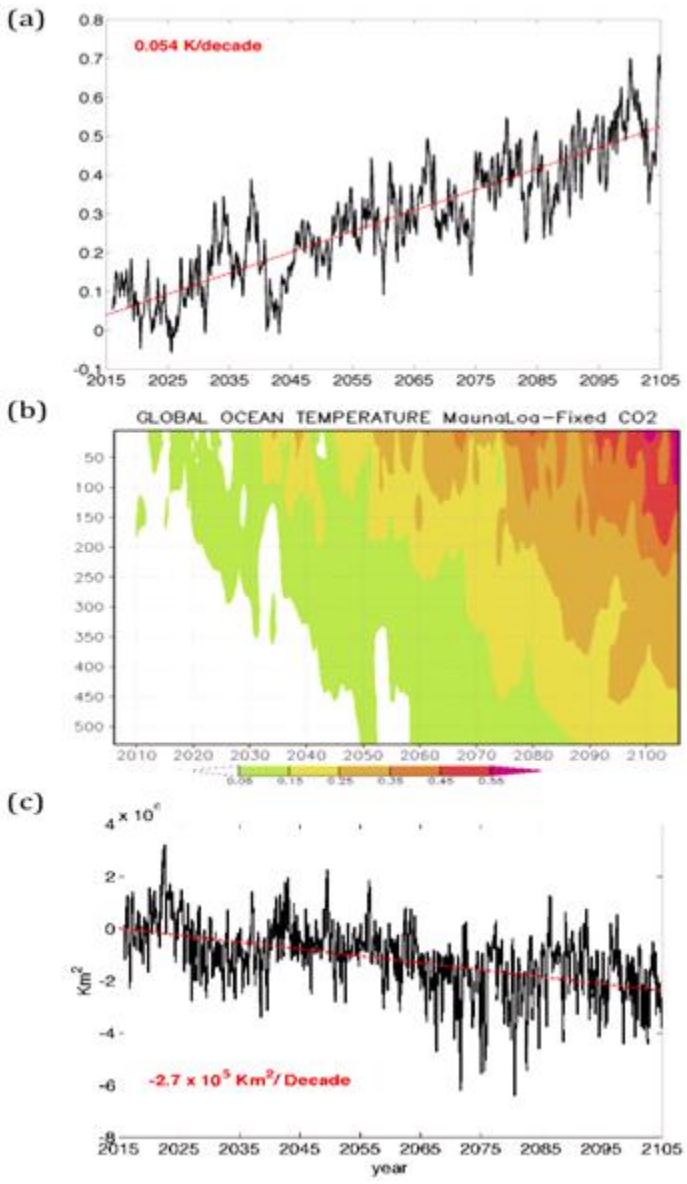

896 Figure 1. Globally averaged, phsics1 minus physics2 residual time series for the
897 centennial2005 runs for (a) Sea Surface Temperature (SST), the red line is the linear fit
898 for the SST time series with acclivity of $+5.4 \times 10^{-2}$ K/decade, (b) Vertical profile of
899 global ocean temperature (K), depicting the propagation of the temperature signal
900 through depth, and (c) Sea ice extent (km^2), the red line is the linear fit for the ice extent
901 time series, with declivity of -2.7×10^5 km^2/decade.

902

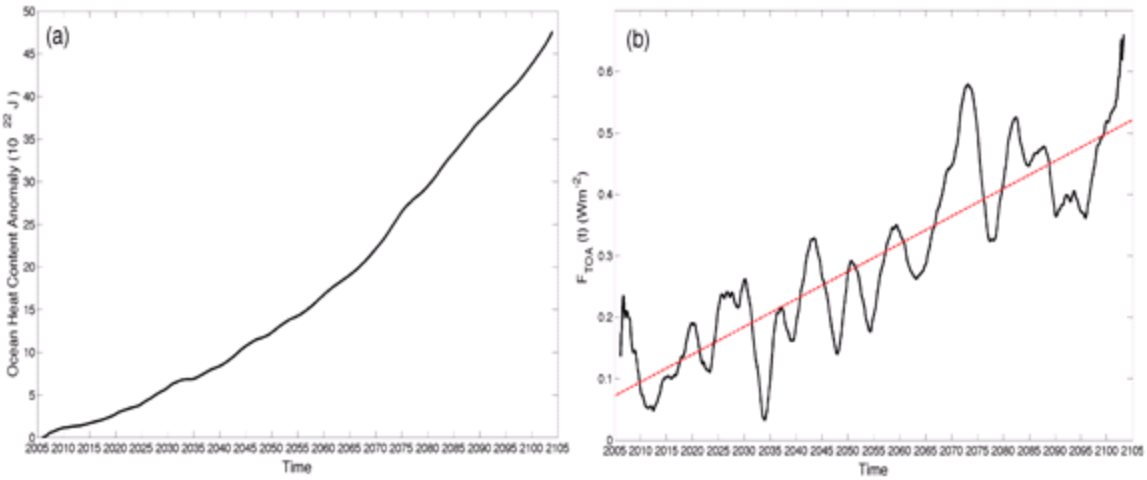

903 Figure 2. 100-year trend for the centennial2005 physics1 minus physics2 residuals in: (a)

904 full depth Ocean Heat Content Anomaly (OHCA) and (b) top-of-atmosphere radiation

905 flux imbalance FTOA implied by the ocean heat content.

906

907

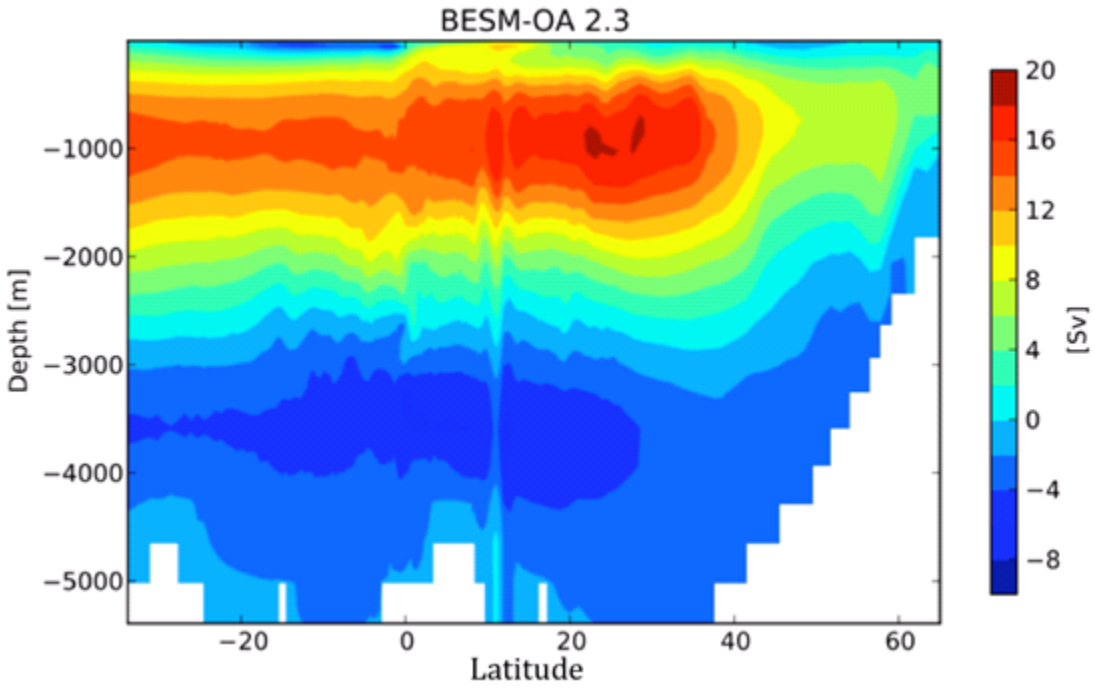

908 Figure 3. Spatial pattern of the Atlantic Meridional Overturning Circulation averaged

909 along 25 years, from year 95 to 120 of centennial1960 physics2 run. This is the vertically

910 cumulative sum of the total zonal transport.

911

912

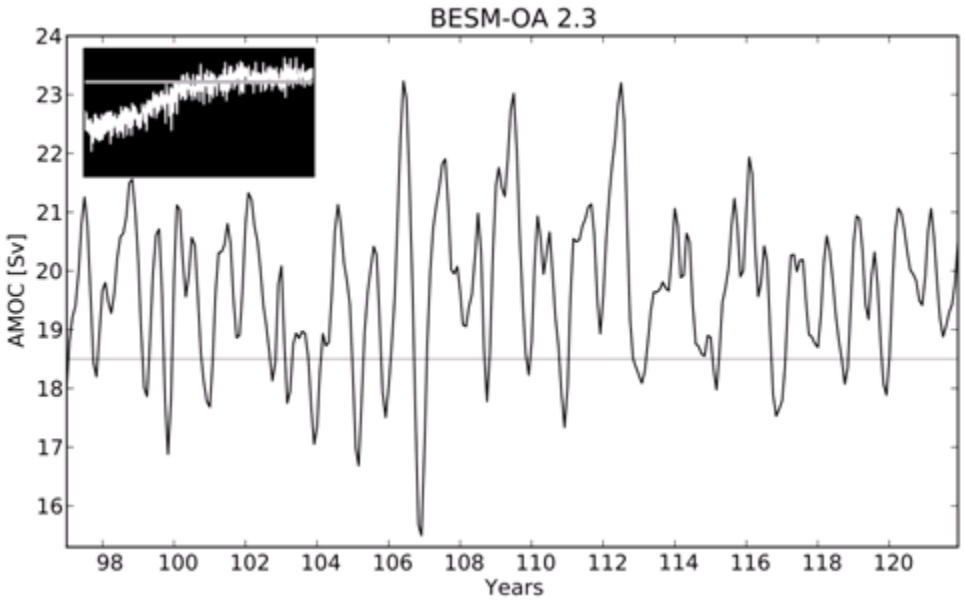

913 Figure 4. Temporal variability of the maximum of the Atlantic meridional overturning
914 Circulation on the BESM-OA2.3 along 25 years of simulation for the centennial1960
915 physics2 run. The smaller frame shows the same maximum along 125 year after the
916 spinup, larger frame shows the temporal variability of the maximum.

917

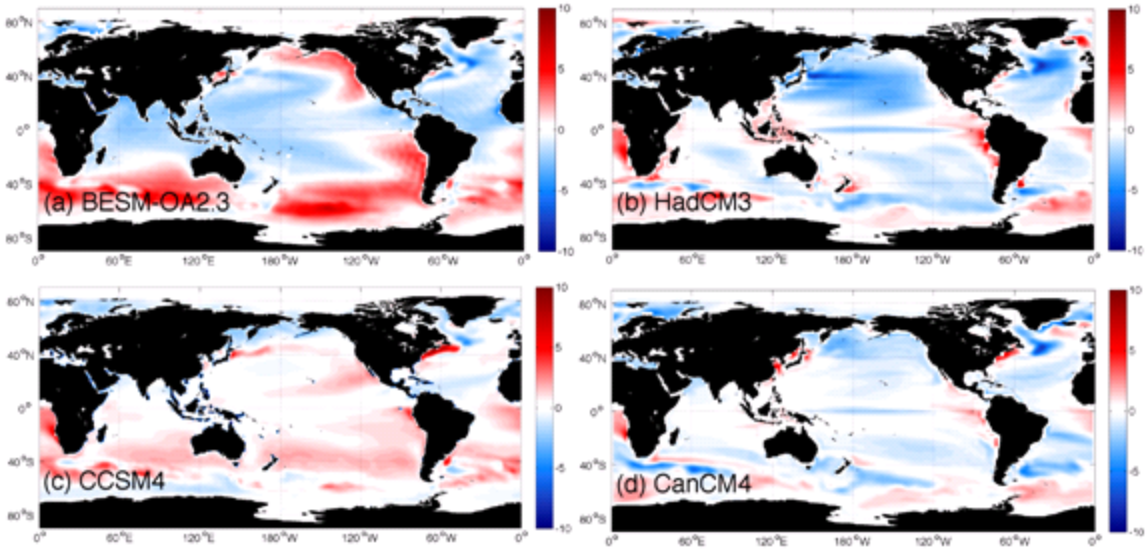

918 Figure 5. Sea surface temperature bias in (a) BESM-OA2.3, (b) Hadley Centre Coupled

919 Model version 3 (HadCM3), (c) NCAR's CCSM4 coupled model, and (d) Canadian

920 CanCM4 coupled model. Units are in K.

921

922

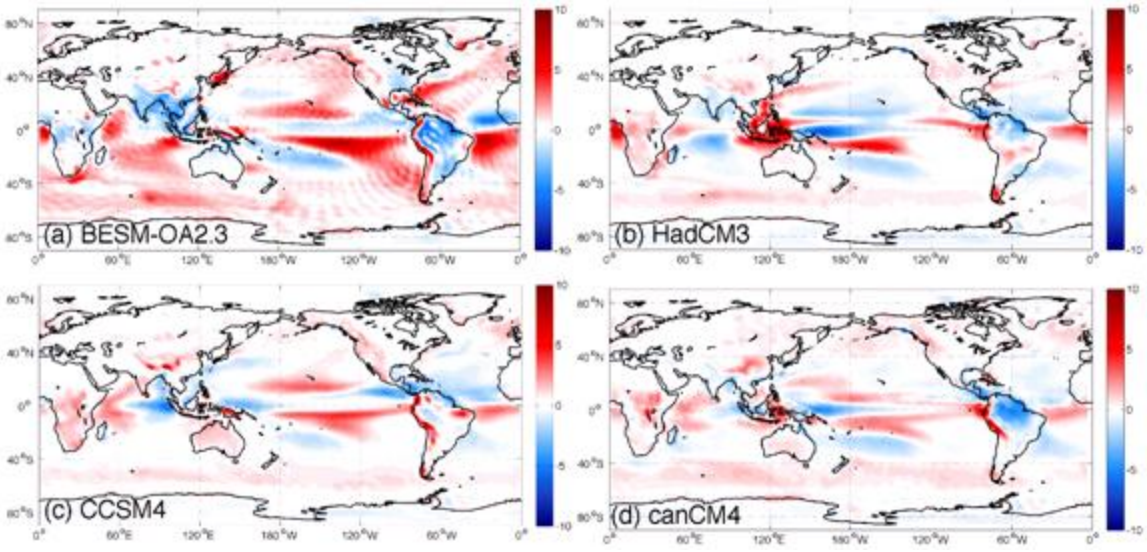

923 Figure 6. Precipitation bias in (a) BESM-OA2.3, (b) Hadley Centre Coupled Model
924 version 3 (HadCM3), (c) NCAR's CCSM4 coupled model, and (d) Canadian CanCM4
925 coupled model. Units are in mm/day.

926

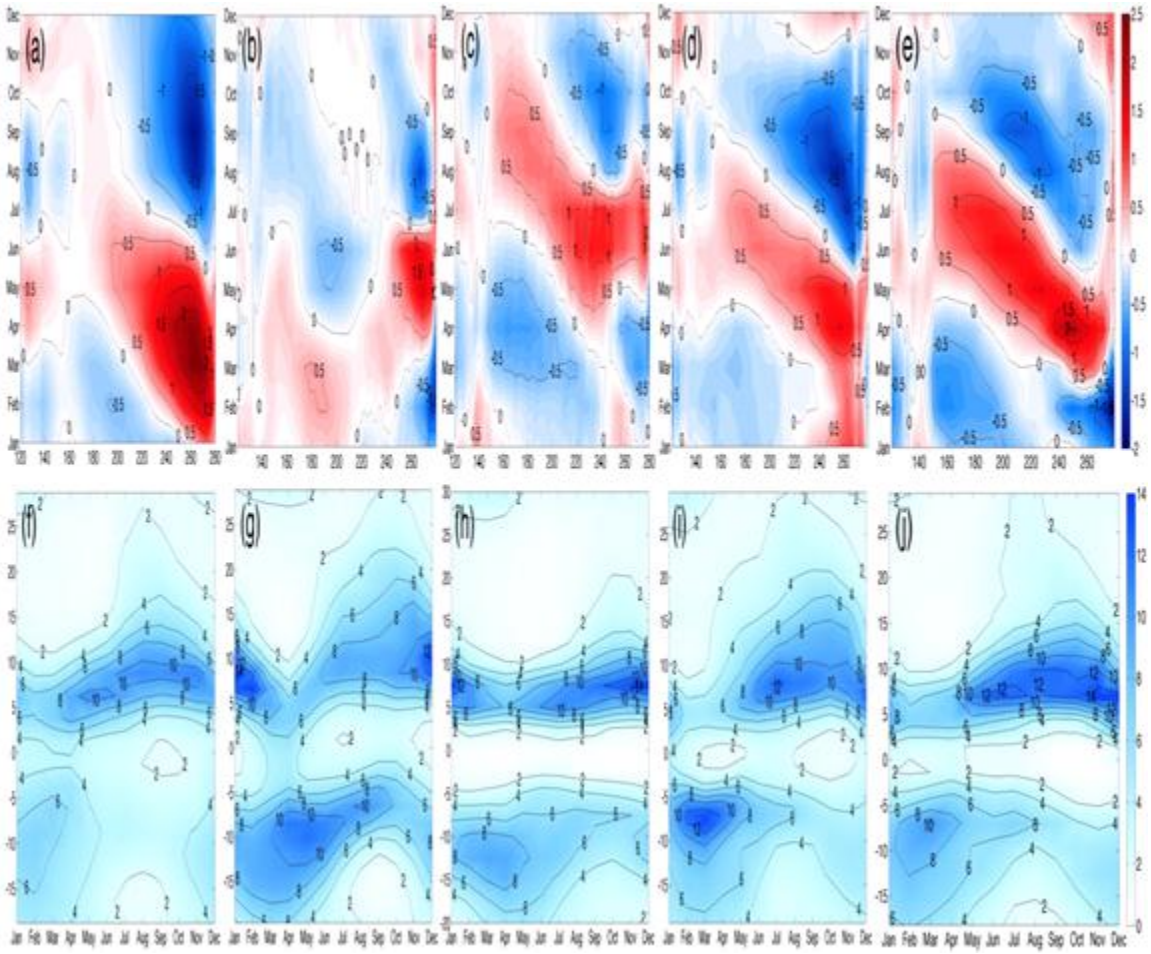

927 Figure 7. The seasonal cycle in equatorial SST (2^{o}S-2^{o}N) in terms of deviations from the
928 respective annual mean in ^{o}C for: (a) OISST, (b) BESM-OA2.3, (c) HadCM3, (d)
929 CCSM4, and (e) CanCM4. The seasonal cycle in precipitation over the eastern Pacific
930 (averaged between 150^{o} and 100^{o}W) plotted against latitude in mm/day for: (f) CMAP,
931 (g) BESM-OA2.3, (h) HadCM3, (i) CCSM4, and (j) CanCM4.

932

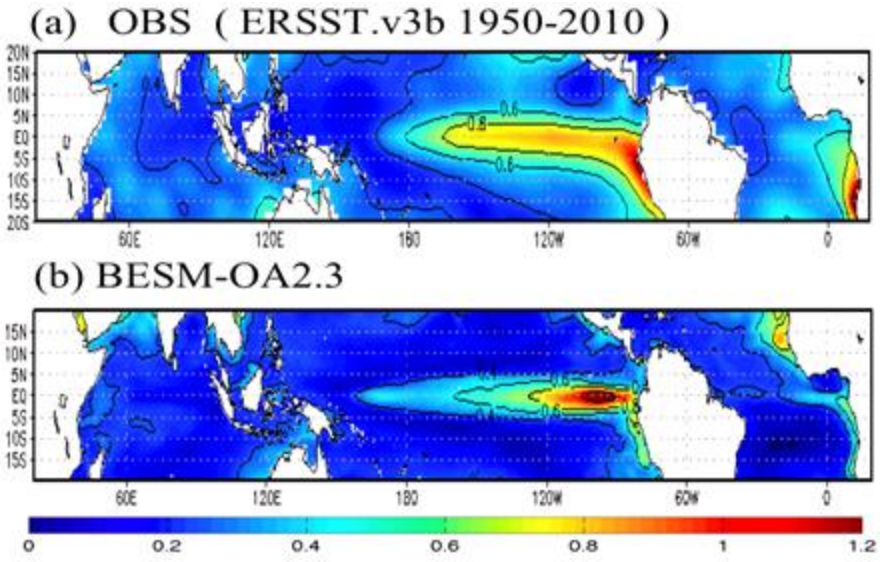

933 Figure 8. Standard deviation of SST anomalies (°C) over the tropics. (a) Observations

934 from ERSSTv3b, years 1950-2010, and (b) BESM-OA2.3 centennial2005 physics2

935 control run.

936

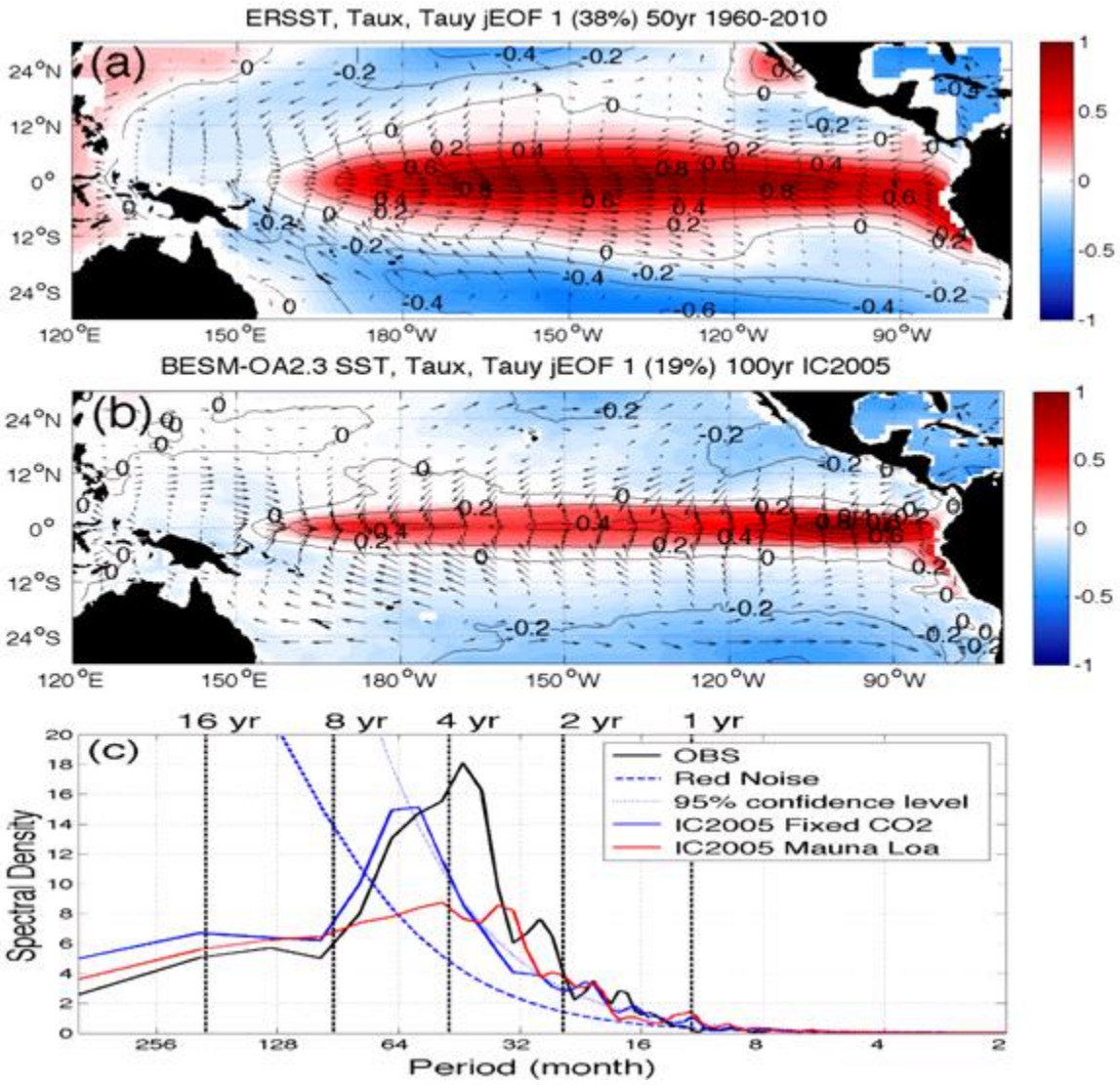

937 Figure 9. First jEOF of SST–Taux–Tauy monthly anomalies in the equatorial Pacific for
938 (a) observations, for the period 1960-2010, and (b) BESM-OA2.3 centennial2005,
939 physics2 control run for the period of the last 90 years of a 100-years run. (c) Power
940 spectra of the monthly PCs time series from observations in solid black, BESM-OA2.3
941 centennial2005 physics2 in solid blue, and BESM-OA2.3 centennial2005 physics1, in
942 solid red. Theoretical red noise spectrum is in dashed blue, 95% confidence level in
943 dotted blue.

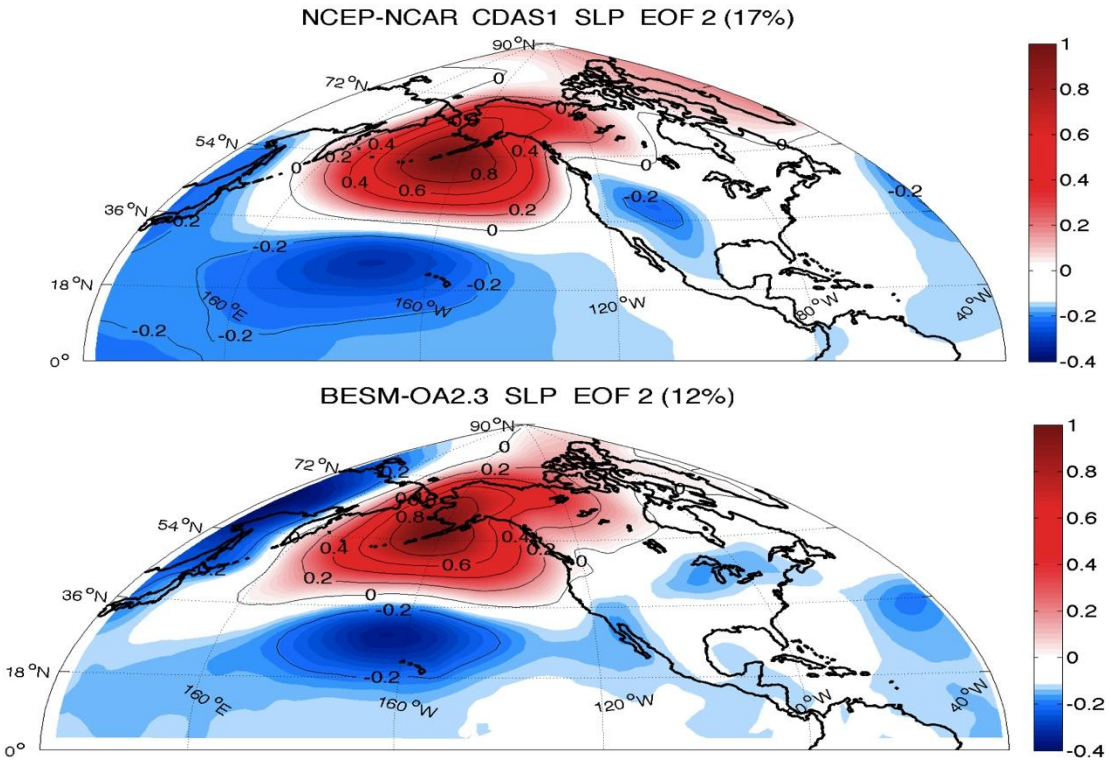

944

945 Figure 10. The PNA teleconnection pattern of positive and negative monthly mean

946 surface pressure anomalies. Second sea level pressure EOF for (top) NCEP-NCAR

947 CDAS1 and (bottom) BESM-OA2.3 centennial2005 physics2 run.

948

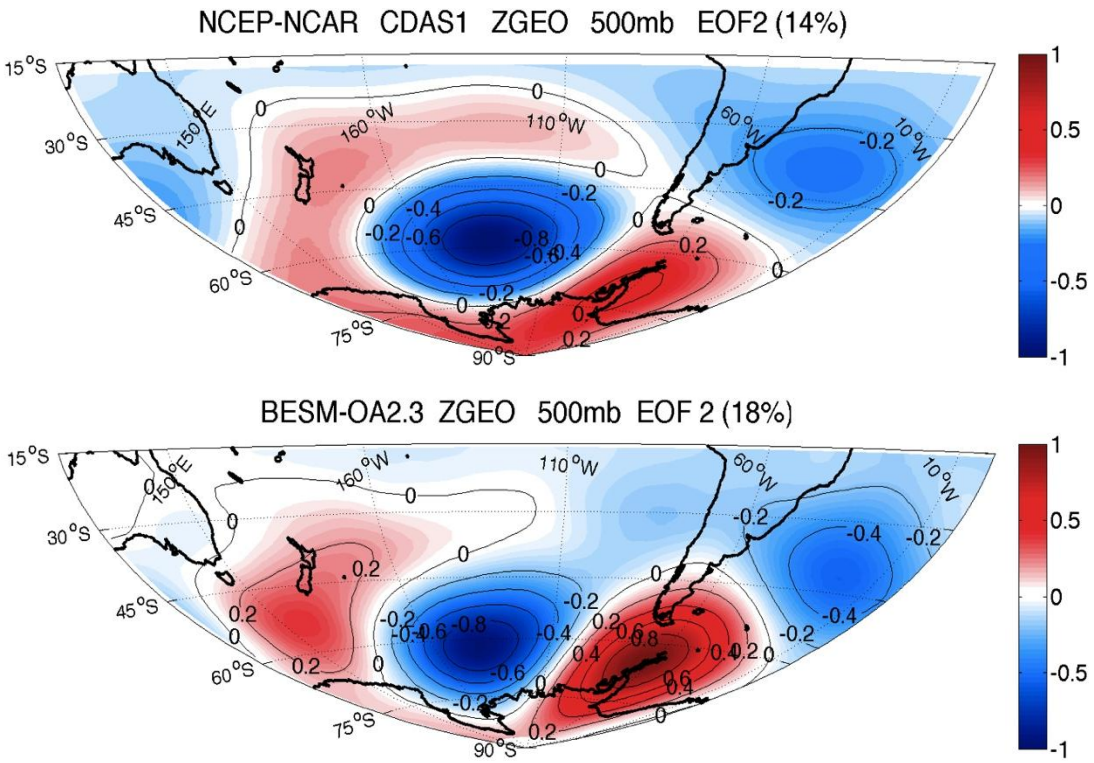

949

950 Figure 11. The PSA teleconnection pattern of positive and negative monthly mean 500-

951 hPa height anomalies. Second 500mb geopotential thickness EOF for (top) NCEP-NCAR

952 CDAS1 and (bottom) BESM-OA2.3 centennial2005 physics2 run.

953

954

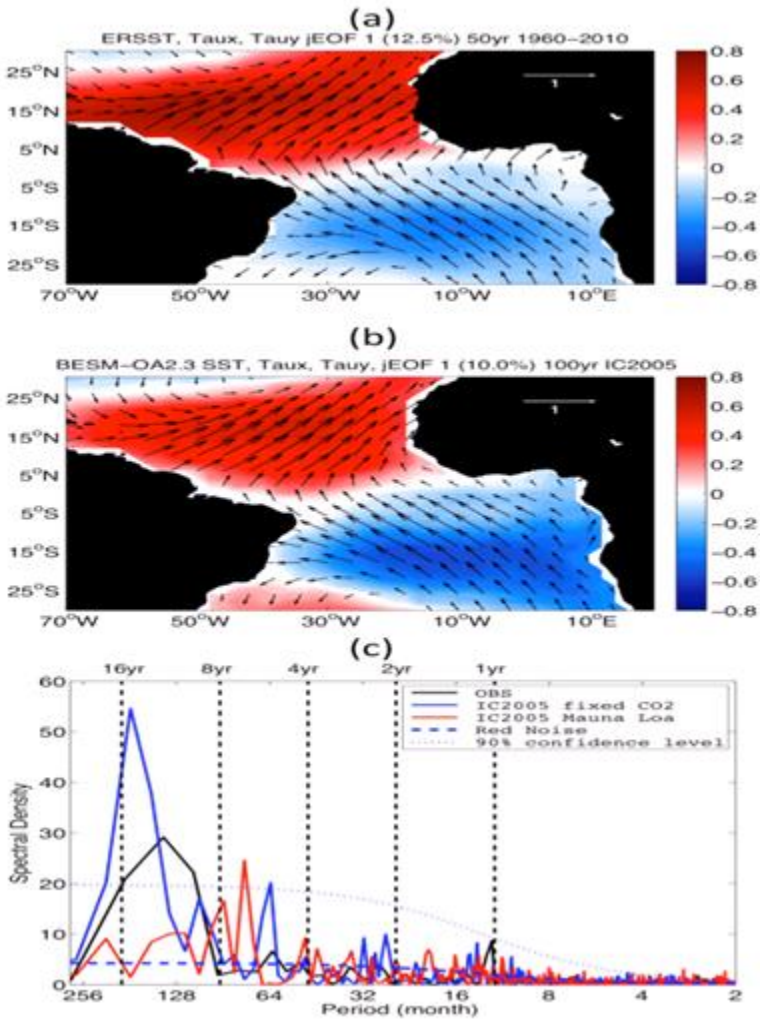

955 Figure 12. Same as Figure 9, but for the Tropical Atlantic between 30 S – 30 N, 70W –

956 20 E.

957

958